doi: 10.82124/CEAS-GNC-2026-041 CEAS-GNC-2026-041

Lunar Lander Variable-Mass Dynamics Modeling Considering Propellant Sloshing

Carl-Johann Winkler Research Assistant, Technische Universität Dresden, Chair of Flight Mechanics and Control, 01307 Dresden, Germany. carl-johann.winkler@tu-dresden.de

Paul Acquatella GNC Systems Engineer, European Space Agency, Guidance, Navigation & Control Section, 2201 AZ Noordwijk, The Netherlands. paul.acquatella@esa.int

Francesco Capolupo GNC Systems Engineer, European Space Agency, Guidance, Navigation & Control Section, 2201 AZ Noordwijk, The Netherlands. francesco.capolupo@esa.int

Harald Pfifer Professor, Technische Universität Dresden, Chair of Flight Mechanics and Control, 01307 Dresden, Germany. harald.pfifer@tu-dresden.de

ABSTRACT

Precision landings on the lunar surface are essential for accessing scientifically valuable sites and enabling future lunar base operations. Achieving such accuracy demands high-fidelity representations of the spacecraft dynamics during early GNC development phases. This work addresses two major challenges in modeling lunar lander dynamics: 1) the accurate capturing of variable-mass dynamics due to rapid propellant consumption, and 2) the characterization of sloshing-induced perturbations, which are strongly dependent on the fill level and the lander's acceleration. Expanding upon a rigid body dynamical model, in this paper we derive a set of nonlinear equations of motion that incorporates both variable-mass effects and sloshing dynamics using a pendulum-based approximation parameterized for spherical tanks. The formulation is modular and scalable, allowing a straightforward integration of multiple tanks and propulsion systems. The model's validity is demonstrated through a simplified lunar lander scenario showing very close alignment with published data on sloshing mode characteristics.

Keywords: GNC Design, Lunar Lander, Variable Mass, Propellant Sloshing, Equations of Motion

Nomenclature

ϕ, θ, ψ	=	Euler angles (roll, pitch, yaw)
η, ξ	=	sloshing angular states
B, I, P	=	body, inertial, pendulum frame
O, S, G, C, F	=	origin, S/C reference, center of gravity, tank center, sloshing propellant
ζ	=	damping rate
ω_0	=	natural frequency
ρ	=	mass particle density
ν	=	kinematic viscosity
a	=	acceleration
$\boldsymbol{e}_{x/y/z}$	=	basis vectors

d = damping coefficient
$\boldsymbol{F}$ = force vector
g = gravitational acceleration
I_{sp} = specific impulse
$\boldsymbol{J}$ = inertia matrix
l = pendulum length
$\boldsymbol{L}$ = angular momentum
m = mass
$\boldsymbol{M}$ = torque vector
$\boldsymbol{n}$ = normal vector
p = pendulum string force
$\boldsymbol{q}$ = quaternion vector
$\boldsymbol{r}_{XY}^{A}$ = direction vector (point X to Y in frame A)
$\boldsymbol{R}_{AB}$ = rotation matrix (frame A to B, s.t. $\boldsymbol{a}^A = \boldsymbol{R}_{AB}\,\boldsymbol{a}^B$)
$\boldsymbol{s}$ = parameterization of points on nozzle cross section
$R_{N/T}$ = nozzle / tank radius
$\boldsymbol{\omega}_{AB}^{B}$ = angular rate vector (frame A with respect to B stated in B)
T = thrust
$\boldsymbol{v}$ = nozzle exhaust velocity vector

1 Introduction

The Apollo 11 landing area on the lunar surface was defined by a target ellipse of about 50 km^2, rendering even large deviations from the nominal trajectory of secondary concern [1]. Today's "New Space Race" aims to greatly improve the touchdown accuracy, now measured in m^2 instead of km^2, to enable scientific research at key locations of interest and establish lunar bases [2]. The increased precision by itself is a difficult feat, further complicated by the need for fully autonomous flight control systems. Lunar landers are similar to launch vehicles in the sense that a large portion of their initial mass is dedicated to propellant, which is then depleted rapidly over the course of the mission. This gives rise to two aspects in need of close consideration: 1) the dynamics of variable-mass systems [3], and 2) the interaction of sloshing propellant with the surrounding tank structure [4].

This paper contributes a methodical derivation of the nonlinear lunar lander equations of motion (EOM) with six degrees of freedom (6-DOF). The EOMs combine both variable-mass effects as well as propellant sloshing. The resulting closed-form structure is scalable and therefore applicable for multi-engine and multi-tank setups.

Section 2 establishes the common elements of lunar lander systems and states the rigid body dynamics. Subsequently, Section 3 addresses the effects of variable-mass systems. Prior work [3, 5] recognizes their importance, specifically in the context of launch vehicles or missiles, and presents analytical derivations of the dynamics. Based on these, force and torque expressions tailored for solid rocket motors firing with established burn profiles are presented in [6]. In this work, we apply the same "principle of solidification" to arrive at closed-form descriptions of the variable-mass effects without a predefined layout. Assuming uniform exhaust flow through a circular engine nozzle, this generalizes the analytical description to accommodate arbitrary nozzle positions and orientations.

The influence of moving liquids within containers have been characterized extensively during the Apollo era, as summarized in [7]. These studies established mechanical replacement models, such as mass-spring-damper systems or pendulums, to approximate the sloshing dynamics. Although sloshing has been accounted for when developing the Saturn V flight control scheme [8, 9], it was not explicitly addressed in the design of the Apollo Landing Module; however, flight data confirmed sloshing effects [4].

Decades later NASA identified a potentially destabilizing interaction of the Altair lunar lander's thrust vectoring system with sloshing oscillations [10]. To aid in the control system design, the ALINA lunar lander adopted a multi-tank sloshing setup using acausal modeling environments for multi-body simulations [11, 12]. Analytical expressions for multi-body dynamics of liquid-propelled launch vehicles to analyze system stability are presented in, e.g., [13] and [14], relying on the aforementioned mechanical sloshing analogies. An equally rigorous derivation for multi-tank lunar lander setups including analytical linearization has recently been presented in [15]. Building upon this foundation, Section 4 implements a pendulum sloshing model for spherical tanks with fill level dependent parameters based on [7]. While generally sufficient for launch vehicles, NASA [16] notes the potential limitations of mechanical replacement models in the specific context of fast maneuvers during lunar missions that evoke nonlinear and secondary terms. Nevertheless, these analogies remain valuable for preliminary Guidance, Navigation, and Control (GNC) design [12, 17].

2 Rigid Body Dynamics of Lander Module with Spherical Tanks

Typical structural layouts of lunar landers feature lightweight and damped landing legs that extend outward to ensure a safe and soft landing while minimizing the risk of tip-over. Maintaining a low center of gravity to improve stability at touchdown, the main engines shall be positioned as low as possible while preserving sufficient ground clearance to allow exhaust gases to disperse laterally without significantly disturbing the lunar regolith during touchdown. Propellant tanks are tightly clustered around the lander's central vertical axis to reduce the moment of inertia. This shortens the propellant feed lines to the engines further, optimizing the configuration and available volumes. Operational equipment and mission payloads can then be strategically placed above and around the tanks, while reaction control thrusters are distributed along the outer structure for sufficient attitude control.

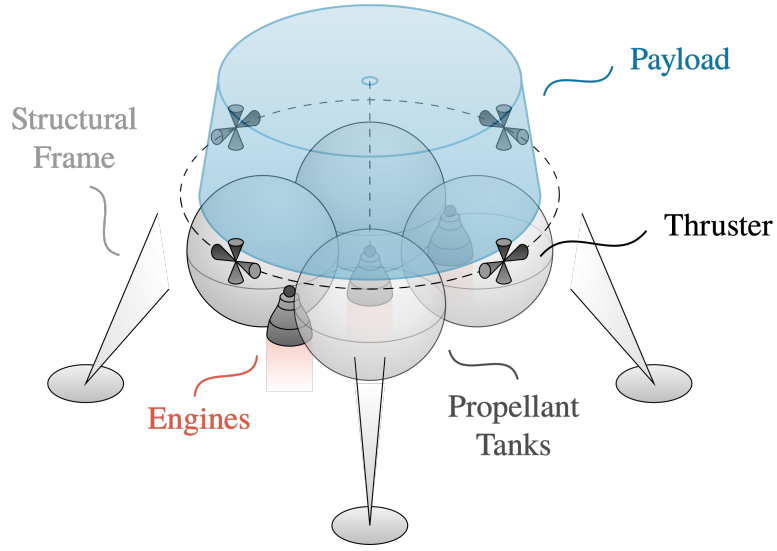

Fig. 1 Typical layout of a lunar lander

We initially focus on a 6-DOF free-floating mass system, depicted in Fig. 1, that attaches a single engine and a single spherical propellant tank. This forms the basis to arrive at the EOMs for a more complex lunar lander setup as in Fig. 1. The selenographic coordinate system in the origin O is chosen as the inertial reference frame I with its z-axis aligned with the Moon's axis of rotation, the x-axis indicating the prime meridian (pointing towards Earth), and the y-axis pointing due East, closing the right-hand system. The lander's reference position S, a static point inside the structure, defines the anchor point of the body frame B. With that, we can define all locations and orientations of the lander's components, such as the tank in C and engine exhaust nozzle in E, with respect to S and B.

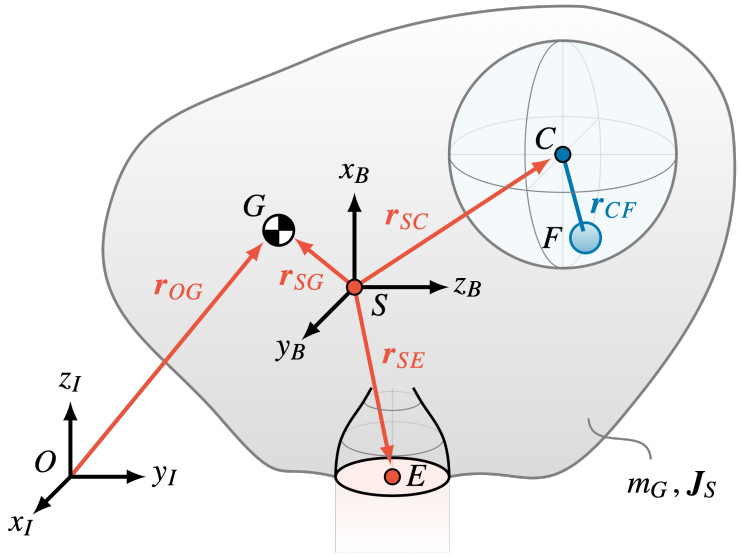

Fig. 2 6-DOF body with a single engine and spherical tank

The current rotation of the lander's body frame B with respect to the inertial frame I is defined by the quaternion $\boldsymbol{q}_{IB} = [q_0 \;\; q_1 \;\; q_2 \;\; q_3]^\top$, where q_0 denotes the scalar component and $(q_1, q_2, q_3)^\top$ the vector component. The corresponding rotation matrix $\boldsymbol{R}_{IB}$ is defined by [18]:

$$\boldsymbol{R}_{IB} = \boldsymbol{C}(\boldsymbol{q}_{IB}) = \begin{bmatrix} 1-2(q_2^2+q_3^2) & 2(q_1q_2-q_0q_3) & 2(q_1q_3+q_0q_2) \\ 2(q_1q_2+q_0q_3) & 1-2(q_1^2+q_3^2) & 2(q_2q_3-q_0q_1) \\ 2(q_1q_3-q_0q_2) & 2(q_2q_3+q_0q_1) & 1-2(q_1^2+q_2^2) \end{bmatrix}. \tag{1}$$

Rotation matrices belong to the special orthogonal group $SO(3)$, which have the property $\boldsymbol{R}_{IB} = \boldsymbol{R}_{BI}^{-1} = \boldsymbol{R}_{BI}^\top$ [19]. The notation is chosen to transform a vector passively, i.e., $\boldsymbol{a}^I = \boldsymbol{R}_{IB}\boldsymbol{a}^B$. The quaternion dynamics $\dot{\boldsymbol{q}}$ according to the Hamilton quaternion multiplication [20] is given as a function of the lander's angular velocity $\boldsymbol{\omega}_{IB}^B$ as:

$$\dot{\boldsymbol{q}} = \frac{1}{2}\boldsymbol{q} \otimes \boldsymbol{\omega}_q \qquad \text{with} \qquad \boldsymbol{\omega}_q = \begin{bmatrix} 0 \\ \boldsymbol{\omega}_{IB}^B \end{bmatrix}. \tag{2}$$

While Euler angles are regularly found in aerospace applications, the use of quaternions is often preferable as it is more computationally efficient and avoids Gimbal Lock. For attitude control designs the Euler angles for roll ϕ, pitch θ, and yaw ψ may still be required and can be recovered by applying Eq. (3) when assuming a Tait-Bryan YXZ rotation sequence (roll angle limited to $\phi \in (-\frac{\pi}{2}, \frac{\pi}{2})$) [18].

$$\begin{bmatrix} \phi \\ \theta \\ \psi \end{bmatrix} = \begin{bmatrix} \operatorname{asin}\Big(2(q_0q_1+q_2q_3)\Big) \\ \operatorname{atan2}\Big(2(q_0q_2-q_1q_3),\; 1-2(q_1^2+q_2^2)\Big) \\ \operatorname{atan2}\Big(2(q_0q_3-q_1q_2),\; 1-2(q_1^2+q_3^2)\Big) \end{bmatrix} \tag{3}$$

With the frames appropriately defined, reexamining Fig. 2 allows us to identify all the forces $\boldsymbol{F}_i$ and moments $\boldsymbol{M}_i$ expected to be acting on the rigid structure. A total of three main influences can be stated:

- $\boldsymbol{F}_g$ / $\boldsymbol{M}_g$ due to gravity acting at the center of gravity G
- $\boldsymbol{F}_{\dot{m}}$/ $\boldsymbol{M}_{\dot{m}}$ due to mass moving inside or exiting the system through the engine nozzle at E
- $\boldsymbol{F}_p$ / $\boldsymbol{M}_p$ due to propellant sloshing modeled as a pendulum attached at the center of the tank C.

We declare that all varying-mass effects are treated as quasi-exogenous forces $\boldsymbol{F}_{\dot{m}}$ and torques $\boldsymbol{M}_{\dot{m}}$ such that we can assume constant mass, center of gravity, and inertia (MCI) parameters; the Newton-Euler approach for constant mass therefore remains valid. The equation for translational motion $\boldsymbol{F} = m\boldsymbol{a}$, valid in the center of gravity G, is adapted to feature the aforementioned contributions as separate forces with:

$$m_G \ddot{\boldsymbol{r}}^I_{OG} = \sum_i \boldsymbol{F}^I_i = \boldsymbol{F}^I_g + \boldsymbol{F}^I_{\dot{m}} + \boldsymbol{F}^I_p. \tag{4}$$

By establishing a basis vector of unit length with $\boldsymbol{e}^I_g = -\boldsymbol{r}^I_{OG}/\|\boldsymbol{r}^I_{OG}\|$, the gravitational force vector can be stated as $\boldsymbol{F}^I_g = m_G g \boldsymbol{e}^I_g$. This provides an easy path to implement a position dependent spherical harmonic gravity model $g = g(\boldsymbol{r}_{OG})$ for the lunar environment; see, e.g., [21].

The rotational dynamics are derived from the angular momentum balance in G, which we express in the body frame by applying $\boldsymbol{L}^I_G = \boldsymbol{R}_{IB}\boldsymbol{L}^B_G$. As gravity acts in G, it will not produce a torque, while any gravity gradient torque is neglected as it is assumed to vanish in the presence of any thrust perturbations induced by the engines; i.e. $\boldsymbol{M}^B_g = 0$.

$$\frac{d}{dt}\boldsymbol{L}^I_G = \sum_i M^I_i \quad \rightarrow \quad \frac{d}{dt}\boldsymbol{L}^B_G + [\boldsymbol{\omega}^B_{IB}\times]\boldsymbol{L}^B_G = \sum_i \boldsymbol{M}^B_i \tag{5}$$

$$\boldsymbol{J}^B_G\dot{\boldsymbol{\omega}}^B_{IB} + [\boldsymbol{\omega}^B_{IB}\times]\boldsymbol{J}^B_G\boldsymbol{\omega}^B_{IB} = \boldsymbol{M}^B_{\dot{m}} + \boldsymbol{M}^B_p \tag{6}$$

Eqs. (4) and (6) establish the basis for deriving the full lunar lander EOMs. The so far undefined contributions originating from varying masses and sloshing propellant are derived in more detail in the subsequent sections.

3 Dynamics of Variable-Mass Systems

An essential aspect of maneuvers performed in the vacuum of space is the realization that significant changes to the trajectory can solely be caused by expelling mass from the system. How the necessary forces and torques are considered or even represented in a dynamical model depends on the specific application and intent. For instance, introducing a simple thrust vector at the engine mounting point (or even in G) may be a practical and viable solution for rapid-prototyping and preliminary studies. However, for more detailed dynamics modeling it is acknowledged that such a simplification is inadequate over the intended time frame of a lunar landing, particularly when rotational motion is considered. This is because the dynamical effects of such variable-mass systems have more terms involved than simply a thrust force and varying mass due to the mass flow rates (propellant consumption). Therefore, the influence of mass redistribution on the system requires a more rigorous treatment, addressed in [5]. Here, the "principle of solidification" is employed, whereby the system is considered with constant MCI properties at any specific point in time and their derivatives with respect to time are zero. Still, the MCI parameters are evolving from one point in time to another [6].

Eke et al. [5] established a set of analytical equations based on Kane's formalism [22] describing the changes that mass particles inflict upon a system's momentum when moving inside or exiting the system's boundaries. The details of the derivation are given in Ref. [5], with only key elements being stated here. Essentially, the rigid body expression $\boldsymbol{F} = m\boldsymbol{a}$ for translational motion is extended to feature three additional forces [5]:

- $\boldsymbol{F}_C$ covering the Coriolis component of the acceleration,
- $\boldsymbol{F}_L$ covering the change of linear momentum due to particle motion inside the system,
- $\boldsymbol{F}_T$ covering the change of linear momentum across the system boundary, commonly portrayed as the aforementioned thrust vector.

$$\boldsymbol{F}_C = -2\int_{\mathcal{B}} \rho(\boldsymbol{\omega}\times\boldsymbol{v})\,dV, \qquad \boldsymbol{F}_L = -\frac{d}{dt}\int_{\mathcal{B}} \rho\boldsymbol{v}\,dV, \qquad \boldsymbol{F}_T = -\int_{\mathcal{S}} \rho\boldsymbol{v}(\boldsymbol{v}\cdot\boldsymbol{n})\,d\mathcal{S} \tag{7}$$

Herein, $\mathcal{B}$ describes the boundary of a variable-mass system, $\mathcal{S}$ its surface area with $\boldsymbol{n}$ being a unit vector normal to it and pointing outwards. A considered mass particle has the density ρ and translational velocity $\boldsymbol{v}$, while $\boldsymbol{\omega}$ describes the rigid body angular velocity, both with respect to an inertial reference frame. Applying Reynolds transport theorem, the Coriolis integral term separates further into a force $\boldsymbol{F}_{C1}$, caused by redistribution of mass inside the boundary, and $\boldsymbol{F}_{C2}$, which considers mass flow across the boundary [5]:

$$\boldsymbol{F}_C = -2\boldsymbol{\omega}\times\frac{d}{dt}\int_{\mathcal{B}} \rho\boldsymbol{r}\,dV - 2\boldsymbol{\omega}\times\int_{\mathcal{S}} \rho\,\boldsymbol{r}(\boldsymbol{v}\cdot\boldsymbol{n})\,d\mathcal{S} = \boldsymbol{F}_{C1} + \boldsymbol{F}_{C2}. \tag{8}$$

During a lunar lander's main thrust phases the internal mass redistribution's influence on the momentum of the lander is generally negligible due to the presence of the large mass ejection across the system boundary at high exhaust velocities, as justified in [5]. Hence, the terms $\boldsymbol{F}_{C1}$ and $\boldsymbol{F}_L$ vanish. To define the remaining contributions we assume two more things:

1) The engine nozzle cross section is stated as a circular disc with radius R_N, a realistic description both for main engines in general as well as most reaction control thrusters. Defining the nozzle disc center location with respect to the center of gravity as $\boldsymbol{r}_{GE} = \boldsymbol{r}_{SE} - \boldsymbol{r}_{SG}$ (see Fig. 3), we can derive the parametrization $\boldsymbol{s}$ in Eq. (9) of every point on the exhaust nozzle surface.

2) The effective exhaust velocity is assumed uniform over and orthogonal to the nozzle cross section, i.e., $\boldsymbol{v}(\boldsymbol{s}) = v_e\boldsymbol{n}$. This simplification is adopted due to the otherwise complex nature of the mass flow exhaust, which is distinct for every engine design and changing continuously along the flight envelope.

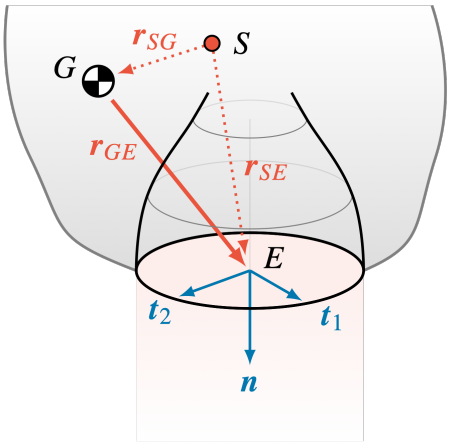

Fig. 3 Engine nozzle cross section

$$\boldsymbol{s}(\boldsymbol{r}_{GE}, R_N) = \boldsymbol{r}_{GE} + \alpha\,(\boldsymbol{t}_1\cos\beta + \boldsymbol{t}_2\sin\beta) \tag{9}$$

$$\text{with} \quad \alpha\in[0, R_N], \quad \beta\in[0, 2\pi], \quad \|\boldsymbol{t}_1\| = \|\boldsymbol{t}_2\| = 1, \quad \boldsymbol{t}_1\times\boldsymbol{t}_2 = \boldsymbol{n}$$

The engine's specific impulse I_{sp} as performance characteristic together with Earth's gravitational constant g_0 allows us to describe the exhaust velocity without atmospheric losses as $v_e = I_{sp}g_0$ such as to explicitly state the thrust $T = -\dot{m}I_{sp}g_0$. The engine orientation with $\boldsymbol{n} = \boldsymbol{R}_{BE}\boldsymbol{e}_x$ applies the rotation matrix notation as above. This yields

$$\boldsymbol{F}_T^B = -\int_{\mathcal{S}} \rho\,\boldsymbol{v}(\boldsymbol{v}\cdot\boldsymbol{n})\,d\mathcal{S} = \dot{m}v_e\boldsymbol{n} = -T\boldsymbol{R}_{BE}\boldsymbol{e}_x. \tag{10}$$

While solving the integral $\int_{\mathcal{S}} (...)\ d\mathcal{S} = \int_0^{2\pi}\int_0^{R_N} \alpha\ (...)\ d\alpha\, d\beta$ for $\boldsymbol{F}_T^B$ is trivial due to the assumption of uniform mass stream, it gets more elaborate for cases that are indeed functions of $\boldsymbol{s}$. For the assumed case of a circular exhaust nozzle, we can state the closed form of the Coriolis component as:

$$\begin{aligned}
\boldsymbol{F}_{C2}^B &= -2\boldsymbol{\omega} \times \int_{\mathcal{S}} \rho\, \boldsymbol{s}(\boldsymbol{v}\cdot\boldsymbol{n})\, d\mathcal{S} \\
&= -2\rho v_e \boldsymbol{\omega} \times \int_0^{2\pi}\int_0^{R_N} \alpha\,(\boldsymbol{r}_{GE} + \alpha\,(\boldsymbol{t}_1\cos\beta + \boldsymbol{t}_2\sin\beta))\, d\alpha\, d\beta \\
&= -2\rho v_e \pi R_N^2 [\boldsymbol{\omega}_{IB}^B\times]\boldsymbol{r}_{GE}^B = \dot{m}\,[\boldsymbol{r}_{GE}^B\times]\boldsymbol{\omega}_{IB}^B \\
\boldsymbol{F}_{C2}^B &= -\frac{T}{g_0 I_{sp}}[\boldsymbol{r}_{GE}^B\times]\boldsymbol{\omega}_{IB}^B. \qquad (11)
\end{aligned}$$

In a similar fashion we can state three contributors to the rotational dynamics of the lander as a result of the motion of mass in an observed mass system $\mathcal{B}$ [5]:

- $\boldsymbol{M}_C$ covering the Coriolis component of the acceleration,
- $\boldsymbol{M}_H$ covering the change of angular momentum due to particle motion inside the system,
- $\boldsymbol{M}_T$ covering the change of angular momentum inflicted by the thrust.

$$\boldsymbol{M}_C = -2\int_{\mathcal{B}} \rho\, \boldsymbol{s}\times(\boldsymbol{\omega}\times\boldsymbol{v})\, dV \qquad \boldsymbol{M}_H = -\frac{d}{dt}\int_{\mathcal{B}} \rho\,(\boldsymbol{s}\times\boldsymbol{v})\, dV \qquad \boldsymbol{M}_T = -\int_{\mathcal{S}} \rho(\boldsymbol{s}\times\boldsymbol{v})(\boldsymbol{v}\cdot\boldsymbol{n})\, d\mathcal{S} \quad (12)$$

Based on the two distinct derivations for the rotational motion in [5], we can expand the Coriolis torque further to obtain Eq. (13), exploiting the expected time derivative of the inertia matrix $\dot{\boldsymbol{J}}$.

$$\boldsymbol{M}_C = -\dot{\boldsymbol{J}}\boldsymbol{\omega} - \int_{\mathcal{S}} \rho\, \boldsymbol{s}\times(\boldsymbol{\omega}\times\boldsymbol{s})\,(\boldsymbol{v}\cdot\boldsymbol{n})\, d\mathcal{S} - \int_{\mathcal{B}} \rho\,\boldsymbol{\omega}\times(\boldsymbol{s}\times\boldsymbol{v})\, dV \quad (13)$$

Both the last term on the right hand side of $\boldsymbol{M}_C$ as well as $\boldsymbol{M}_H$ can be neglected for steady state relative motion of particles, which is a valid assumption for the presented application due to long durations of near constant thrust (see, e.g., [23]). The remaining integral in $\boldsymbol{M}_C$ describes the so-called Jet Damping, a torque that is (for most rocket configurations) opposing rotational motion transversal to the exhaust stream. For a circular exhaust nozzle with uniform exhaust flow, the integral leads to a closed form of the Jet Damping torque as:

$$\begin{aligned}
\boldsymbol{M}_{jet}^B &= -\int_{\mathcal{S}} \rho\, \boldsymbol{s}\times(\boldsymbol{\omega}\times\boldsymbol{s})\,(\boldsymbol{v}\cdot\boldsymbol{n})\, d\mathcal{S} = -\rho v_e\left[\int_{\mathcal{S}} (\boldsymbol{s}\cdot\boldsymbol{s})\,\boldsymbol{\omega}\, d\mathcal{S} - \int_{\mathcal{S}} (\boldsymbol{s}\cdot\boldsymbol{\omega})\,\boldsymbol{s}\, d\mathcal{S}\right] \\
&= -\rho v_e\left[\int_0^{2\pi}\int_0^{R_N} \alpha\,(\boldsymbol{s}\cdot\boldsymbol{s})\,\boldsymbol{\omega}\, d\alpha\, d\beta - \int_0^{2\pi}\int_0^{R_N} \alpha\,(\boldsymbol{s}\cdot\boldsymbol{\omega})\,\boldsymbol{s}\, d\alpha\, d\beta\right] \\
&= -\dot{m}\underbrace{\left[\left(\|\boldsymbol{r}_{GE}^B\|^2 + \frac{R_N^2}{2}\right)\boldsymbol{I}_3 - (\boldsymbol{r}_{GE}^B\boldsymbol{r}_{GE}^{B\top}) - \frac{R_N^2}{4}(\boldsymbol{I}_3 - \boldsymbol{R}_{BE}\boldsymbol{e}_x\boldsymbol{e}_x^\top\boldsymbol{R}_{BE}^\top)\right]}_{=\boldsymbol{A}_{jet}^B}\boldsymbol{\omega}_{IB}^B \\
\boldsymbol{M}_{jet}^B &= \frac{T}{g_0 I_{sp}}\boldsymbol{A}_{jet}^B\,\boldsymbol{\omega}_{IB}^B. \qquad (14)
\end{aligned}$$

Lastly, the thrust stated in Eq. (10) acting in E naturally generates a torque around G.

$$\boldsymbol{M}_T^B = -\int_{\mathcal{S}} \rho(\boldsymbol{s}\times\boldsymbol{v})(\boldsymbol{v}\cdot\boldsymbol{n})\, d\mathcal{S} = \dot{m}v_e[\boldsymbol{r}_{GE}\times]\boldsymbol{R}_{BE}\boldsymbol{e}_x = -T[\boldsymbol{r}_{GE}\times]\boldsymbol{R}_{BE}\boldsymbol{e}_x \quad (15)$$

To summarize, we can define the force inflicted upon the rigid body due to mass flowing through a single engine by adding Eqs. (10) and (11) together. Similarly, the thrust and Jet Damping torques caused by a single engine can be calculated using Eqs. (14) and (15), respectively, while the inertia tensor's derivative stated in Eq. (13) only appears once for the entire system, independent of the number of engines.

4 Pendulum Sloshing Approximation

Estimating the behavior of moving liquids in a container for a lunar lander guidance and control application is relevant due to the large momentum that the propellant carries relative to the lander's dry MCI properties. While sloshing in microgravity is a concern for attitude control during coast phases, our focus lies on high-g applications such as for launchers and lunar descent burns. In those cases, sloshing oscillations might cause system instability, if not properly managed.

Numerous publications documenting the interaction of sloshing propellant with its surrounding structure have been published following its recognition in the early years of space flight; see, e.g., [8, 17, 24]. The general consensus is to section the total propellant into a sloshing and a static portion, shown in Fig. 4. The static portion is added to the rigid MCI properties described in Section 2, whereby the exchange of momentum caused by the propellant being transferred between the systems is assumed negligible (see Section 3). The sloshing propellant portion can be mathematically approximated as a superposition of multiple damped oscillatory modes. For preliminary analyses it is customary to only consider the first mode, as this is the one having the largest effect on the vehicle dynamics [17]. The oscillatory system can then be modeled as either a second-order mass-spring-damper system or a damped pendulum, forming a multi-body problem when attached to the 6-DOF rigid structure [13].

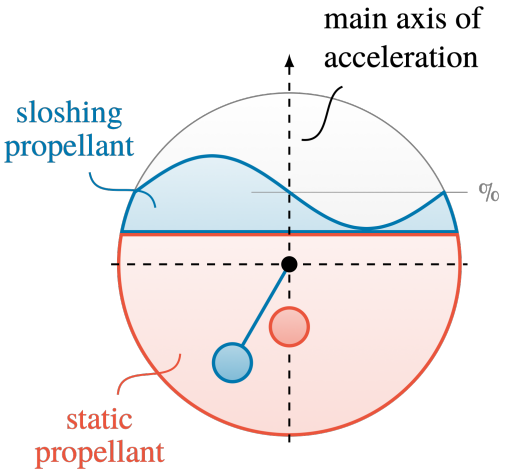

Fig. 4 Separating current propellant mass (%) into sloshing (—) and static (—) portions with pendulum sloshing approximation

This second-order system's characteristics are dependent on a number of design parameters related to the lander: tank shape and size, propellant type, current acceleration, etc. An extensive overview of the dependencies has been collected in [7] and republished in an updated form in [25]. We choose to focus on the dynamics derivation using a pendulum approximation fixed at the center of a spherical tank, as the pendulum's natural frequency similarly varies with the current acceleration a and pendulum length l through $\omega_0 = \sqrt{a/l}$, while the spherical shape helps to conceive the concept of assuming the central attachment point [26]. Nonetheless, spherical tanks are a special case of cylindrical tanks with spherical end caps, also regularly found in lunar landers. For our purposes, these come at the cost of more elaborate derivations (e.g., by not assuming a fixed attachment), without adding much insight.

It is important to note that the considered pendulum approximation cannot accurately represent effects due to swirling motion of the propellant. This is acceptable since major rolling motion (rotation about the primary axis of acceleration in Fig. 4) of the lander during the approach is not to be expected until just before touchdown, if at all.

Deriving the pendulum dynamics starts at the tank's center C, a known and fixed distance $\boldsymbol{r}_{SC}^{B}$ from the lander's reference point S. Assuming the main axis of acceleration is parallel to the body x-axis, there is no need to define a new orientation frame in C, i.e., for any rotation we can apply the body frame B, with B' only denoting the translated coordinates. The sloshing pendulum is then attached in C and we define a pendulum frame P such that its x-axis goes through C and F with $\boldsymbol{r}_{CF}^{P} = -l\boldsymbol{e}_x$. The frame P is described by sequencing a rotation of η around the shifted body frame's $y_{B'}$-axis and rotating by ξ around the new x-axis, as depicted in Fig. 5. Analogous to the rigid body case, this leads to the definition of the following rotation matrix:

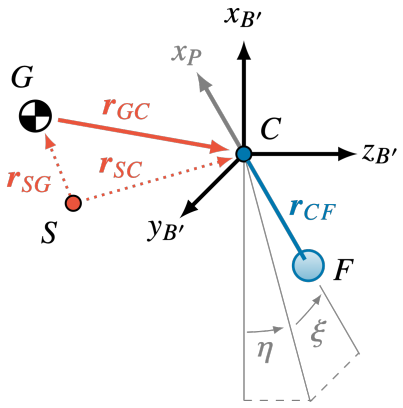

Fig. 5 Pendulum frame rotation

$$\boldsymbol{R}_{BP} = \boldsymbol{R}_y(\eta)\,\boldsymbol{R}_z(\xi) = \begin{bmatrix} \cos\eta & 0 & \sin\eta \\ 0 & 1 & 0 \\ -\sin\eta & 0 & \cos\eta \end{bmatrix} \begin{bmatrix} \cos\xi & -\sin\xi & 0 \\ \sin\xi & \cos\xi & 0 \\ 0 & 0 & 1 \end{bmatrix} = \begin{bmatrix} \cos\eta\cos\xi & -\cos\eta\sin\xi & \sin\eta \\ \sin\xi & \cos\xi & 0 \\ -\sin\eta\cos\xi & \sin\eta\sin\xi & \cos\eta \end{bmatrix} \tag{16}$$

as well as the associated angular velocities $\boldsymbol{\omega}_{BP}^{P}$ and acceleration $\dot{\boldsymbol{\omega}}_{BP}^{P}$:

$$\boldsymbol{\omega}_{BP}^{P} = \dot{\eta}\boldsymbol{y}_B^P + \dot{\xi}\boldsymbol{z}_P^P = \dot{\eta}\boldsymbol{R}_{BP}\boldsymbol{e}_y + \dot{\xi}\boldsymbol{e}_z = \begin{bmatrix} \dot{\eta}\sin\xi \\ \dot{\eta}\cos\xi \\ \dot{\xi} \end{bmatrix} \xrightarrow{d/dt} \dot{\boldsymbol{\omega}}_{BP}^{P} = \begin{bmatrix} \ddot{\eta}\sin\xi + \dot{\eta}\dot{\xi}\cos\xi \\ \ddot{\eta}\cos\xi - \dot{\eta}\dot{\xi}\sin\xi \\ \ddot{\xi} \end{bmatrix}. \tag{17}$$

We can now derive the acceleration $\ddot{\boldsymbol{r}}_{OF}$: from Fig. 5 we combine the tank's location $\boldsymbol{r}_{SC}^{B}$ and the center of gravity $\boldsymbol{r}_{SG}^{B}$ to get $\boldsymbol{r}_{GC}^{B} = \boldsymbol{r}_{SC}^{B} - \boldsymbol{r}_{SG}^{B}$. We further simplify the derivation setting $\dot{\boldsymbol{r}}_{CF}^{P} \approx 0$, assuming that the contribution of the length derivative to the pendulum's overall dynamics is negligible, justified at the end of this section.

$$\boldsymbol{r}_{OF}^{I} = \boldsymbol{r}_{OG}^{I} + \boldsymbol{R}_{IB}\boldsymbol{r}_{GC}^{B} + \boldsymbol{R}_{IP}\boldsymbol{r}_{CF}^{P} \tag{18a}$$

$$\dot{\boldsymbol{r}}_{OF}^{I} = \dot{\boldsymbol{r}}_{OG}^{I} + \boldsymbol{R}_{IB}[\boldsymbol{\omega}_{IB}^{B}\times]\boldsymbol{r}_{GC}^{B} + \boldsymbol{R}_{IB}[\boldsymbol{\omega}_{IB}^{B}\times]\boldsymbol{R}_{BP}\boldsymbol{r}_{CF}^{P} + \boldsymbol{R}_{IP}[\boldsymbol{\omega}_{BP}^{P}\times]\boldsymbol{r}_{CF}^{P} \tag{18b}$$

$$\begin{aligned} \ddot{\boldsymbol{r}}_{OF}^{I} = \ddot{\boldsymbol{r}}_{OG}^{I} &+ \boldsymbol{R}_{IB}\left(\underline{[\boldsymbol{\omega}_{IB}^{B}\times]^2} + \underset{\cdots}{[\dot{\boldsymbol{\omega}}_{IB}^{B}\times]}\right)\boldsymbol{r}_{GC}^{B} + \boldsymbol{R}_{IB}\left(\underline{[\boldsymbol{\omega}_{IB}^{B}\times]^2} + \underset{\cdots}{[\dot{\boldsymbol{\omega}}_{IB}^{B}\times]}\right)\boldsymbol{R}_{BP}\boldsymbol{r}_{CF}^{P} + \ldots \\ &+ \boldsymbol{R}_{IP}\left(\underline{[\boldsymbol{\omega}_{BP}^{P}\times]^2} + \underset{\cdots}{[\dot{\boldsymbol{\omega}}_{BP}^{P}\times]}\right)\boldsymbol{r}_{CF}^{P} + \underline{2\boldsymbol{R}_{IB}[\boldsymbol{\omega}_{IB}^{B}\times]\boldsymbol{R}_{BP}[\boldsymbol{\omega}_{BP}^{P}\times]\boldsymbol{r}_{CF}^{P}} \end{aligned} \tag{18c}$$

In Eq. (18c) we identify the characteristic centrifugal (—) and Euler terms ($\cdots$) of the outer and inner rotation (rigid structure and pendulum, respectively), as well as the Coriolis term (– –) due to the superposition of both rotations. We introduce the sloshing propellant mass m_F and collect all acting forces in F by means of the Newton-Euler formalism, namely gravity $\boldsymbol{F}_g$ (assuming $\boldsymbol{r}_{OF} \approx \boldsymbol{r}_{OG}$), a damping force $\boldsymbol{F}_d$ (linearly depending on the pendulum's angular velocity), and the string force $\boldsymbol{F}_{p^+}$ (orienting the acting scalar force p in space).

$$\ddot{\boldsymbol{r}}_{OF}^{I} = \frac{\boldsymbol{F}_g^I}{m_F} + \frac{\boldsymbol{R}_{IP}\boldsymbol{F}_d^P}{m_F} + \frac{\boldsymbol{R}_{IP}\boldsymbol{F}_{p^+}^P}{m_F} \quad \text{with} \quad \boldsymbol{F}_g^I = m_F g\boldsymbol{e}_g^I, \quad \boldsymbol{F}_d^P = \begin{bmatrix} 0 \\ d\dot{\xi} \\ -d\dot{\eta} \end{bmatrix}, \quad \boldsymbol{F}_{p^+}^P = \begin{bmatrix} p \\ 0 \\ 0 \end{bmatrix} \tag{19}$$

Substituting $\ddot{\boldsymbol{r}}^I_{OF}$ from Eq. (18c) into Eq. (19), we sort the resulting formula such that only the contributions containing the string force $\boldsymbol{F}^P_{p^+}$ and the pendulum angular acceleration $\dot{\boldsymbol{\omega}}^P_{BP}$ are on the left side, while all other terms are on the right. Changing frames from inertial to pendulum frame by multiplication with $\boldsymbol{R}_{PI}$ and introducing the basis vectors $\boldsymbol{e}_{x/y/z}$, the left side can then be restated as:

$$\begin{aligned}\frac{\boldsymbol{F}^P_{p^+}}{m_F} - [\dot{\boldsymbol{\omega}}^P_{BP}\times]\boldsymbol{r}^P_{CF} &= \begin{bmatrix} p/m_F \\ 0 \\ 0 \end{bmatrix} + l \begin{bmatrix} 0 \\ \ddot{\xi} \\ -\ddot{\eta}\cos\xi + \dot{\eta}\dot{\xi}\sin\xi \end{bmatrix} \\ &= p\,\frac{1}{m_F}\boldsymbol{e}_x + \ddot{\xi} l \boldsymbol{e}_y - \ddot{\eta}\, l\cos\xi \boldsymbol{e}_z + l\dot{\eta}\dot{\xi}\cos\xi \boldsymbol{e}_z. \end{aligned} \tag{20}$$

From this, a reformulation giving three decoupled equations for the scalar string force p and the angular accelerations $\ddot{\eta}$ and $\ddot{\xi}$ can be obtained. The latter two describe the state of the pendulum, whereas the former describes the sloshing force ultimately acting on the rigid body lander.

$$\begin{bmatrix} p \\ \ddot{\xi} \\ \ddot{\eta} \end{bmatrix} = \begin{bmatrix} m_F & 0 & 0 \\ 0 & 1/l & 0 \\ 0 & 0 & -1/(l\cos\xi) \end{bmatrix} \left(\boldsymbol{R}_{PI}\ddot{\boldsymbol{r}}^I_{OG} - \boldsymbol{R}_{PB}[\boldsymbol{r}^B_{GC}\times]\dot{\boldsymbol{\omega}}^B_{IB} - [\boldsymbol{r}^P_{CF}\times]\boldsymbol{R}_{BP}\dot{\boldsymbol{\omega}}^B_{IB} + \boldsymbol{\epsilon}^P \right) \tag{21}$$

with
$$\begin{aligned}\boldsymbol{\epsilon}^P = {} & \boldsymbol{R}_{PB}[\boldsymbol{\omega}^B_{IB}\times]^2\boldsymbol{r}^B_{GC} + \boldsymbol{R}_{PB}[\boldsymbol{\omega}^B_{IB}\times]^2\boldsymbol{R}_{BP}\boldsymbol{r}^P_{CF} + [\boldsymbol{\omega}^P_{BP}\times]^2\boldsymbol{r}^P_{CF} + \ldots \\ & + 2\boldsymbol{R}_{PB}[\boldsymbol{\omega}^B_{IB}\times]\boldsymbol{R}_{BP}[\boldsymbol{\omega}^P_{BP}\times]\boldsymbol{r}^P_{CF} - \boldsymbol{R}_{PI}g\boldsymbol{e}^I_g - \frac{\boldsymbol{F}^P_d}{m_F} - l\dot{\eta}\dot{\xi}\cos\xi\boldsymbol{e}_z \end{aligned}$$

Recognizing that $\boldsymbol{e}_x^\top[\boldsymbol{r}^P_{CF}\times] = 0$, the notation for the scalar sloshing force p can be further shortened to

$$p = m_F\boldsymbol{e}_x^\top\left(\boldsymbol{R}_{PI}\ddot{\boldsymbol{r}}^I_{OG} - \boldsymbol{R}_{PB}[\boldsymbol{r}^B_{GC}\times]\dot{\boldsymbol{\omega}}^B_{IB} + \boldsymbol{\epsilon}^P\right). \tag{22}$$

Eq. (21) establishes the means to define the multi-body problem; nevertheless, the fill level dependent parameters are missing that divide the propellant into a sloshing and a static portion. To address that, the collected data in [7, 25], originally presented as functions of fill height ratio h/R_T, is recalculated for our purposes into dependencies on the propellant mass percentage by applying the geometry of a spherical volume. Fig. 6 (a) states the mass of both static and sloshing portions in relation to the current total propellant in the tank m_C, while Fig. 6 (b) relates these to the (initial) full tank propellant mass $m_{C,0}$. The length of the static propellant mass portion in Fig. 6 (c) indicates the distance of its center of gravity from the center of the tank (see Fig. 4). As mentioned earlier, we assume this to be collinear with the primary axis of acceleration with the liquid being stationary at the bottom of the tank. Hence, its center of gravity is geometrically linked to its actual mass such that its MCI parameters can simply be stored in a lookup table.

Evaluating Fig. 6 (b) and (c) we recognize that in regions where the sloshing pendulum length derivative $\dot{\boldsymbol{r}}^P_{CF} = \dot{l}_F\boldsymbol{e}_x$ would be largest, the actual mass contributing in the sloshing motion is the smallest, and vice versa. This validates our initial hypothesis that the length derivative to the pendulum's overall dynamics can be neglected. To establish the damping constant d in Eq. (19) such that ζ in Fig. 6 (d) is fulfilled, we first calculate the non-gravitational acceleration at the tank's center

$$a = \|\ddot{\boldsymbol{r}}^I_{OC} - g\boldsymbol{e}^I_g\| = \|\ddot{\boldsymbol{r}}^I_{OG} + \boldsymbol{R}_{IB}\left([\boldsymbol{\omega}^B_{IB}\times]^2 + [\dot{\boldsymbol{\omega}}^B_{IB}\times]\right)\boldsymbol{r}^B_{GC} - g\boldsymbol{e}^I_g\| \tag{23}$$

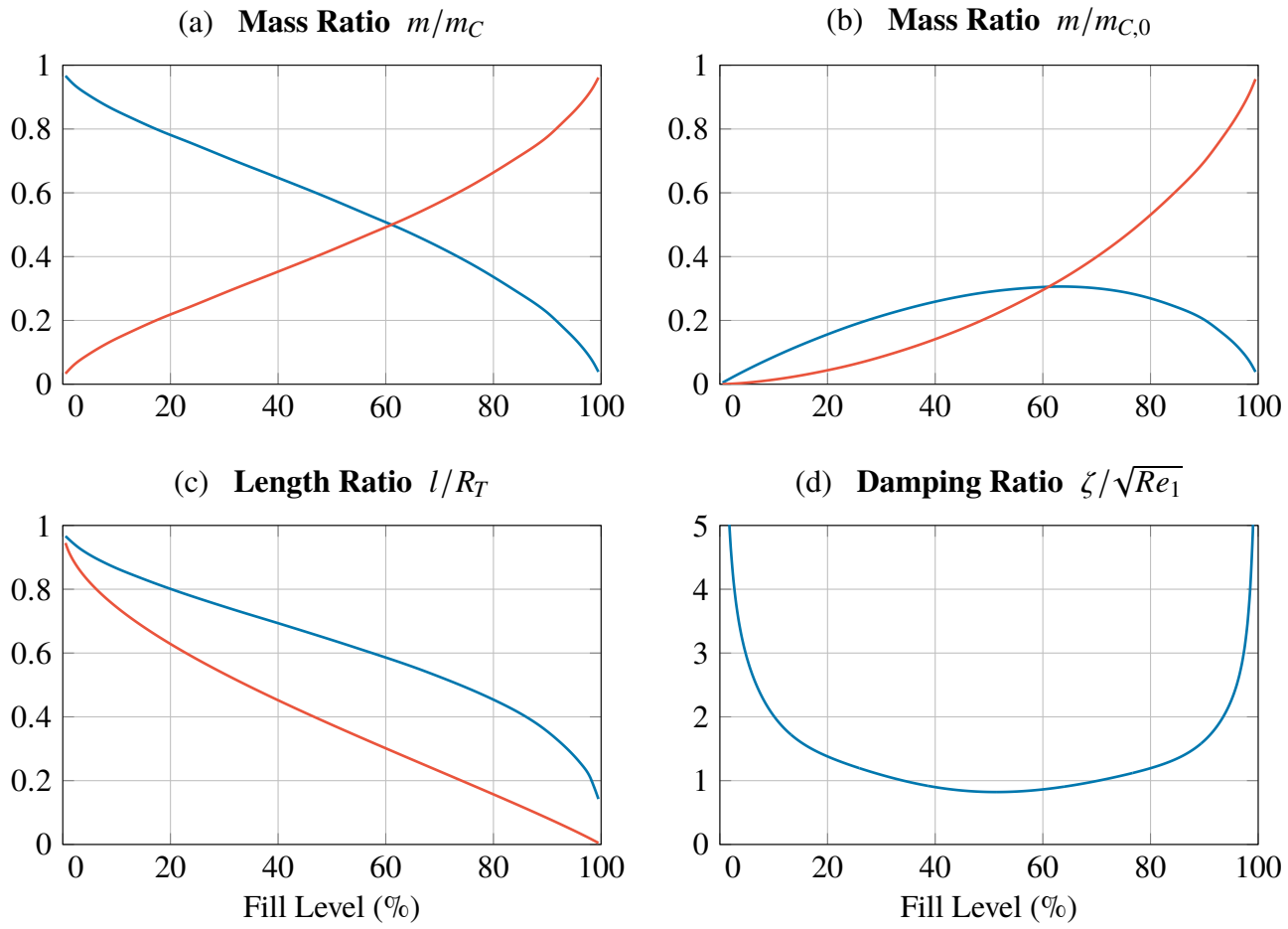

Fig. 6 Fill level dependent parameters for sloshing (—) and static (—) propellant mass portion

to evaluate the dimensionless parameter Re_1 stated in Eq. (24), which also depends on the propellant's kinematic viscosity ν and a characteristic length, defined as the tank's diameter $L = 2R_T$ [7, 25].

$$Re_1 = \frac{\nu}{\sqrt{aL^3}} \tag{24}$$

With the sloshing specific parameters m_F and l gathered from Fig. 6 (b) and (c) based on the current propellant mass inside the tank, we assume a generic damped second-order pendulum to state the damping moment as $F_d l = (dl)\,\dot{\varphi} = (2ml^2\zeta\omega_0)\dot{\varphi}$. Further expanding by using $\omega_0 = \sqrt{a/l}$, we obtain:

$$d = 2m_F\zeta\sqrt{a\,l}. \tag{25}$$

Fig. 6 (d) approximates Eq. (2.9) in [25] using a higher-order polynomial to eliminate the discontinuity at 50% fill level. We recognize that for close to full and nearly empty fill levels the damping increases. This is due to, for one, the small actual propellant mass participating in the sloshing motion such that surface tension and tank wall friction become more pronounced and, secondly, the participating mass decreasing faster than the static portion at low levels of propellant. The lookup data presented in Fig. 6 also provide meaningful information for mission planning. In between 40...80% fill level the absolute sloshing mass peaks while experiencing the least damping, thus exerting the largest force on the structure, as predicted in Ref. [27]. Therefore, fast attitude maneuvers during these periods are best avoided to prevent large excitations of the mode.

5 Multi-body Nonlinear Equations of Motion

In the preceding sections we first established the rigid body dynamics subject to exogenous forces of various origins. In a landing burn scenario, these origins are predominantly mass being exhausted from the system, next to the potential of sloshing propellant interacting with the structure. Both phenomena have been analyzed such that we can collect them as forces and torques influencing the rigid body dynamics with:

$$\boldsymbol{F}^I_{\dot{m}} = \boldsymbol{R}_{IB}\left(\boldsymbol{F}^B_{C2} + \boldsymbol{F}^B_T\right) = -T\left(\frac{\boldsymbol{R}_{IB}}{g_0 I_{sp}}[\boldsymbol{r}^B_{GE}\times]\boldsymbol{\omega}^B_{IB} + \boldsymbol{R}_{IE}\boldsymbol{e}_x\right) \tag{26}$$

$$\boldsymbol{F}^I_p = -\boldsymbol{R}_{IP}\boldsymbol{F}^P_{p^+} = -m_F\boldsymbol{R}_{IP}\boldsymbol{e}_x\boldsymbol{e}_x^\top\left(\boldsymbol{R}_{PI}\ddot{\boldsymbol{r}}^I_{OG} - \boldsymbol{R}_{PB}[\boldsymbol{r}^B_{GC}\times]\dot{\boldsymbol{\omega}}^B_{IB} + \boldsymbol{\epsilon}^P\right) \tag{27}$$

$$\boldsymbol{M}^B_{\dot{m}} = \boldsymbol{M}^B_C + \boldsymbol{M}^B_T = -\dot{\boldsymbol{J}}^{\boldsymbol{B}}_{\boldsymbol{G}}\boldsymbol{\omega}^B_{IB} + T\left(\frac{\boldsymbol{A}^B_{jet}}{g_0 I_{sp}}\boldsymbol{\omega}^B_{IB} - [\boldsymbol{r}^B_{GE}\times]\boldsymbol{R}_{BE}\boldsymbol{e}_x\right) \tag{28}$$

$$\boldsymbol{M}^B_p = -[\boldsymbol{r}^B_{GC}\times]\boldsymbol{R}_{BP}\boldsymbol{F}^P_{p^+} = -m_F[\boldsymbol{r}^B_{GC}\times]\boldsymbol{R}_{BP}\boldsymbol{e}_x\boldsymbol{e}_x^\top\left(\boldsymbol{R}_{PI}\ddot{\boldsymbol{r}}^I_{OG} - \boldsymbol{R}_{PB}[\boldsymbol{r}^B_{GC}\times]\dot{\boldsymbol{\omega}}^B_{IB} + \boldsymbol{\epsilon}^P\right). \tag{29}$$

Note that the string force $\boldsymbol{F}_{p^+}$, originally derived at the sloshing mass in F, must cancel out with an opposing string force $\boldsymbol{F}_p$ in C, leading to the sign change in Eq. (27). Recall that Eqs. (4), (6) and (21) state the fundamental equations to calculate the derivatives $\ddot{\boldsymbol{r}}^{\boldsymbol{I}}_{\boldsymbol{OG}}$ and $\dot{\boldsymbol{\omega}}^{\boldsymbol{B}}_{\boldsymbol{IB}}$ of the 6-DOF rigid body motion as well as the pendulum states $\ddot{\xi}$ and $\ddot{\eta}$. The natural step now is to fuse the gained formulae by substituting in Eqs. (26) to (29) for the varying-mass and sloshing forces and torques. Sorting the equations such that all contributions by the state derivatives $\ddot{\boldsymbol{r}}^I_{OG}$, $\dot{\boldsymbol{\omega}}^B_{IB}$, $\ddot{\xi}$, and $\ddot{\eta}$ are on the left side and all the remaining on the right establishes a structured form $\boldsymbol{\mathcal{M}}\ddot{\boldsymbol{x}} = \boldsymbol{u}$ as in:

$$\left[\begin{array}{cc|cc}
m_G\boldsymbol{I}_3 + m_F\boldsymbol{R}_{IP}\boldsymbol{e}_x\boldsymbol{e}_x^\top\boldsymbol{R}_{PI} & -m_F\boldsymbol{R}_{IP}\boldsymbol{e}_x\boldsymbol{e}_x^\top\boldsymbol{R}_{PB}[\boldsymbol{r}^B_{GC}\times] & \boldsymbol{\emptyset}_{3\times1} & \boldsymbol{\emptyset}_{3\times1} \\
m_F[\boldsymbol{r}^B_{GC}\times]\boldsymbol{R}_{BP}\boldsymbol{e}_x\boldsymbol{e}_x^\top\boldsymbol{R}_{PI} & \boldsymbol{J}^B_G - m_F[\boldsymbol{r}^B_{GC}\times]\boldsymbol{R}_{BP}\boldsymbol{e}_x\boldsymbol{e}_x^\top\boldsymbol{R}_{PB}[\boldsymbol{r}^B_{GC}\times] & \boldsymbol{\emptyset}_{3\times1} & \boldsymbol{\emptyset}_{3\times1} \\
\hline
-\boldsymbol{e}_y^\top\boldsymbol{R}_{PI} & \boldsymbol{e}_y^\top\left(\boldsymbol{R}_{PB}[\boldsymbol{r}^B_{GC}\times] + [\boldsymbol{r}^P_{CF}\times]\boldsymbol{R}_{BP}\right) & l & 0 \\
-\boldsymbol{e}_z^\top\boldsymbol{R}_{PI} & \boldsymbol{e}_z^\top\left(\boldsymbol{R}_{PB}[\boldsymbol{r}^B_{GC}\times] + [\boldsymbol{r}^P_{CF}\times]\boldsymbol{R}_{BP}\right) & 0 & -l\cos\xi
\end{array}\right]\left[\begin{array}{c}
\ddot{\boldsymbol{r}}^{\boldsymbol{I}}_{\boldsymbol{OG}} \\
\dot{\boldsymbol{\omega}}^{\boldsymbol{B}}_{\boldsymbol{IB}} \\
\hline
\ddot{\xi} \\
\ddot{\eta}
\end{array}\right]$$

$$\ldots = \left[\begin{array}{c}
m_G g\boldsymbol{e}^I_g - T\left(\boldsymbol{R}_{IE}\boldsymbol{e}_x + \frac{\boldsymbol{R}_{IB}}{g_0 I_{sp}}[\boldsymbol{r}^B_{GE}\times]\boldsymbol{\omega}^B_{IB}\right) - m_F\boldsymbol{R}_{IP}\boldsymbol{e}_x\boldsymbol{e}_x^\top\boldsymbol{\epsilon}^P \\
-[\boldsymbol{\omega}^B_{IB}\times]\boldsymbol{J}^B_G\boldsymbol{\omega}^B_{IB} - \dot{\boldsymbol{J}}^B_G\boldsymbol{\omega}^B_{IB} + \frac{T}{g_0 I_{sp}}\left(\boldsymbol{A}^B_{jet}\boldsymbol{\omega}^B_{IB} - [\boldsymbol{r}^B_{GE}\times]\boldsymbol{R}_{BE}\boldsymbol{e}_x\right) - m_F[\boldsymbol{r}^B_{GC}\times]\boldsymbol{R}_{BP}\boldsymbol{e}_x\boldsymbol{e}_x^\top\boldsymbol{\epsilon}^P \\
\hline
\boldsymbol{e}_y^\top\boldsymbol{\epsilon}^P \\
\boldsymbol{e}_z^\top\boldsymbol{\epsilon}^P
\end{array}\right]. \tag{30}$$

The pendulum state derivatives in Eq. (30) are coupled to the rigid 6-DOF derivatives unidirectionally. Referencing Eqs. (19), (21) and (22), the algebraic loop is avoided since p includes only the x-value of $\boldsymbol{F}_d$, which is indeed zero. We can therefore exploit the sparse structure to first calculate the rigid body accelerations required for evaluating the damping in Eq. (23) to subsequently calculate the sloshing state evolution. The structure of Eq. (30) further comes in handy recognizing the repeatable pattern presented in Eq. (31) when introducing additional propellant tanks (marked in blue) and engines or thrusters (marked in red). Recall that the inertia's time derivative in Eq. (28) only appears once, while all the other variable-mass terms are evaluated for each engine or thruster separately.

$$\left[\begin{array}{cc|ccc} m_G \boldsymbol{I}_3 + \sum_{i=1}^{n} \boldsymbol{\mathcal{F}}_i & \sum_{i=1}^{n} \boldsymbol{\mathcal{P}}_i & & \boldsymbol{\emptyset}_{6\times 2n} & \\ \sum_{i=1}^{n} \boldsymbol{\mathcal{Q}}_i & \boldsymbol{J}_G^B + \sum_{i=1}^{n} \boldsymbol{\mathcal{J}}_i & & & \\ \hline \boldsymbol{\mathcal{R}}_1 & & \boldsymbol{\mathcal{L}}_1 & \boldsymbol{\emptyset}_{2\times 2} & \cdots \\ \boldsymbol{\mathcal{R}}_2 & & \boldsymbol{\emptyset}_{2\times 2} & \boldsymbol{\mathcal{L}}_2 & \\ \vdots & & \vdots & & \ddots \end{array}\right] \left[\begin{array}{c} \ddot{\boldsymbol{x}}_{S/C} \\ \hline \ddot{\boldsymbol{x}}_{F1} \\ \ddot{\boldsymbol{x}}_{F2} \\ \vdots \end{array}\right] = \left[\begin{array}{c} \boldsymbol{\mathcal{G}} + \sum_{j=1}^{m} \boldsymbol{\mathcal{T}}_j + \sum_{i=1}^{n} \boldsymbol{\mathcal{E}}_i \\ \hline \boldsymbol{\mathcal{U}}_1 \\ \boldsymbol{\mathcal{U}}_2 \\ \vdots \end{array}\right] \tag{31}$$

Showcasing the applicability of the derived EOMs for GNC designs, we envision the simplified lunar lander illustrated in Fig. 7 with a single tank and a single engine in a monopropellant configuration. The propellant characteristics loosely resemble those of ASCENT (formerly AF-M315E) [28]. The center of gravity of the rigid vehicle as well as the inertial frame's origin are collinear with the body x-axis such that no torques are generated. We do not consider any rotational motion, as the lunar lander dynamics are inherently unstable and describing a control design exceeds the scope of this publication. We instead evaluate the fill level dependent sloshing mode characteristics from a MATLAB® / Simulink® implementation applying numerical linearization techniques. Relevant lander parameters are listed in Tab. 1, while the others can be chosen somewhat arbitrarily, provided the aforementioned collinearity is respected.

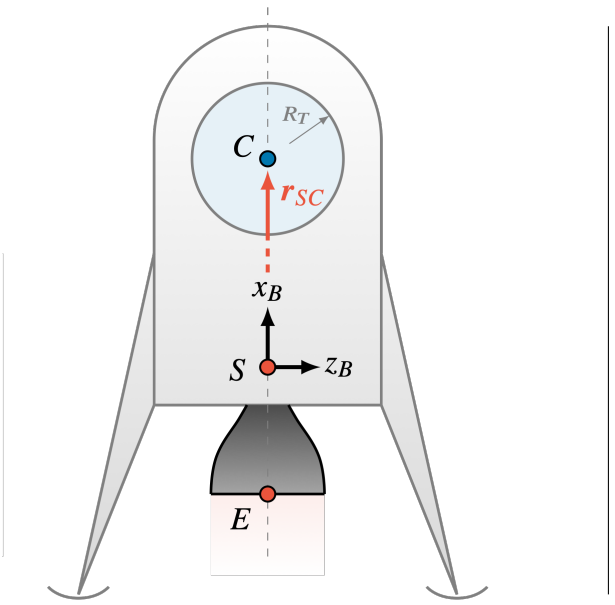

Fig. 7 Example lunar lander

Table 1 Example parameters.

Parameter	Value
m_S	1 000 kg
$m_{C,0}$	1 000 kg
$\boldsymbol{r}_{SC}^B$	$[1 \;\; 0 \;\; 0]^\top$ m
$\boldsymbol{r}_{SE}^B$	$[-1 \;\; 0 \;\; 0]^\top$ m
$\boldsymbol{R}_{BE}$	diag($[-1 \;\; 1 \;\; -1]$)
R_T	0.55 m
ν	$1.67 \cdot 10^{-5}$ kg/s
g	1.57 m/s^2
g_0	9.81 m/s^2
I_{sp}	300 s
T	3 000 N

The linearization was performed at fill levels of 1 to 99% with 1% increments. The results in Fig. 8 (a) and (b) yield damping ratios and natural frequencies of the sloshing mode in expected regions, while Fig. 8 (c) shows very close alignment with the analytically predicted values for a normalized first sloshing mode frequency stated in [7, 25] and validated for spherical tanks using CFD in [29]. This underlines the validity of the presented pendulum implementation to quantify the impact of sloshing propellant on spacecraft in high-g scenarios.

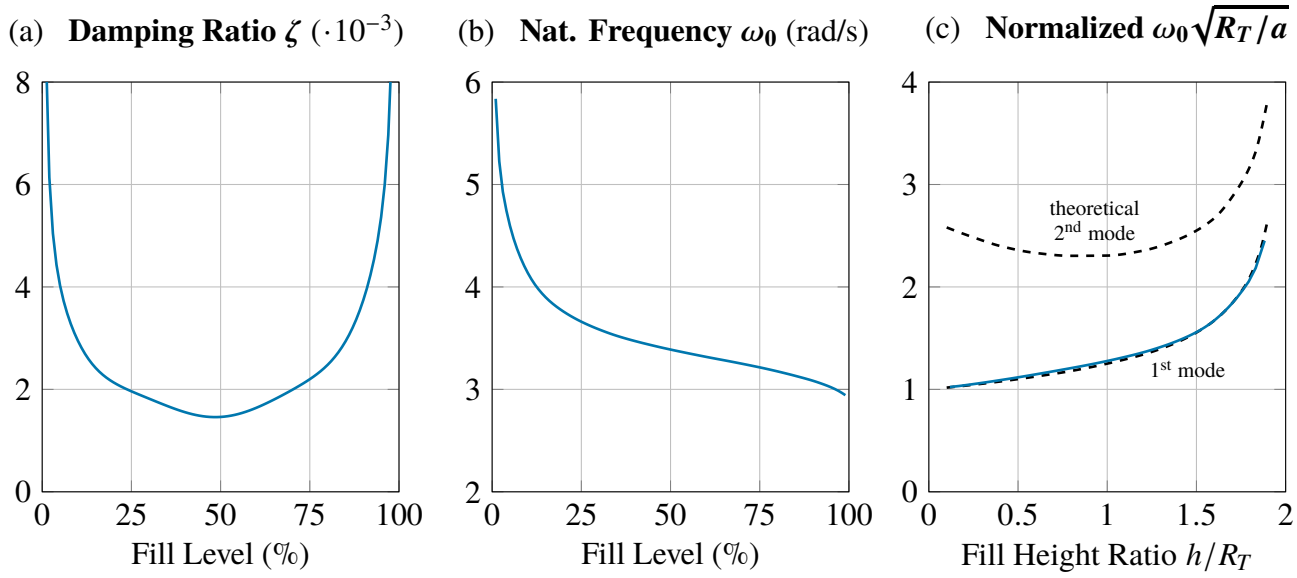

Fig. 8 Fill level dependent sloshing mode damping and frequency characteristics derived using linearized models (——) and compared to analytical predictions (– –) based on [7, 25]

6 Conclusion

It was the objective of this paper to derive a dynamic model suitable for the simulation of the terminal descent phase of a lunar lander, with a focus on accurate consideration and representation of key physical phenomena. This model is motivated by supporting a substantiated and robust GNC development. The lunar lander dynamics modeling was faced with two main challenges: 1) accurate capturing of the variable-mass dynamics due to (rapid) propellant consumption, and 2) the impact of the effects and perturbations due to liquid sloshing in a spherical container, which exhibit strong dependence on fill level and the current acceleration acting on the lander. By extending a rigid-body dynamics model, this work derived a set of equations of motion that incorporate both variable-mass effects and sloshing dynamics using a pendulum-based approximation. The formulation is structured to be modular and scalable, allowing straightforward integration of multiple tanks and propulsion systems into a nonlinear simulation environment. The validity of the approach was demonstrated through implementation in MATLAB® / Simulink® where the resulting sloshing characteristics showed very good agreement with published data for the first sloshing mode. This confirmed the accuracy of the pendulum approximation and the suitability of the model for early-phase GNC design and analysis.

Acknowledgments

This work is part of the OSIP co-funded research titled *Perception Enabled Model Free Control for Space System Landing* that received funding by the European Space Agency under contract No. 4000143985/24/NL/MGu/my. The view expressed in this paper can in no way be taken to reflect the official opinion of the European Space Agency.

Declaration of Use of Artificial Intelligence

Artificial intelligence was used for grammar and spelling checks.

References

[1] F. V. Bennett. Apollo lunar descent and ascent trajectories. NASA Technical Memorandum NASA-TM-X-58040, NASA Manned Spacecraft Center, Houston, TX, USA, Mar. 1970.

[2] Diego De Rosa, Ben Bussey, Joshua T. Cahill, Tobias Lutz, Ian A. Crawford, Terence Hackwill, Stephan van Gasselt, Gerhard Neukum, Lars Witte, Andy McGovern, Peter M. Grindrod, and James D. Carpenter. Characterisation of potential landing sites for the european space agency's lunar lander project. *Planetary and Space Science*, 74(1):224–246, Dec. 2012. ISSN: 0032-0633. doi: 10.1016/j.pss.2012.08.002.

[3] L. Meirovitch. The general motion of a variable-mass flexible rocket with internal flow. NASA Contractor Report NASA-CR-1528, University of Cincinnati, OH, USA, Feb. 1970.

[4] Mission Evaluation Team, Manned Spacecraft Center. Apollo 11 mission report: Preflight, flight, and postflight of Apollo 11. NASA Technical Memorandum NASA-TM-X-62633, NASA, Manned Spacecraft Center, Houston, TX, USA, Nov. 1969.

[5] F. O. Eke. Dynamics of variable mass systems. NASA Contractor Report NASA/CR-1998-208246, Department of Mechanical and Aeronautical Engineering, University of California, CA, USA, Jan. 1998.

[6] B. Gäßler, L. E. Briese, P. Acquatella, P. Simplício, S. Bennani, and M. Casasco. Variable-mass dynamics implementations in multi-physics environment for reusable launcher simulations. In *Proceedings of the 9th European Conference for Aerospace Sciences*, Lille, France, June 2022. doi: 10.13009/EUCASS2022-6124.

[7] H. N. Abramson. The dynamic behavior of liquids in moving containers. NASA Special Publication SP-106, NASA Science and Technical Information Division, Washington, D.C., USA, 1966.

[8] H. F. Bauer. Stability boundaries of liquid-propelled space vehicles with sloshing. *AIAA Journal*, 1(7), July 1963. doi: 10.2514/3.1861.

[9] J. A. Frosch and D. P. Vallely. Saturn AS-501/S-IC flight control system design. *Journal of Spacecraft and Rockets*, 4(8):1003–1009, Aug. 1967. ISSN: 1533-6794. doi: 10.2514/3.29009.

[10] A. Lee, A. Strahan, R. Tanimoto, and A. Casillas. Preliminary characterization of the Altair lunar lander slosh dynamics and some implications for the thrust vector control design. In *AIAA Guidance, Navigation, and Control Conference*. American Institute of Aeronautics and Astronautics, June 2010. doi: 10.2514/6.2010-7721.

[11] J. L. R. Gutierrez, S. Farì, and M. Winter. Control system design for the ALINA lunar lander. In *Proceedings of the 72nd International Astronautical Congress (IAC), Dubai, United Arab Emirates*, pages 25–29, 2021.

[12] S. Farì, D. Seelbinder, and S. Theil. Advanced GNC-oriented modeling and simulation of vertical landing vehicles with fuel slosh dynamics. *Acta Astronautica*, 204:294–306, Mar. 2023. ISSN: 0094-5765. doi: 10.1016/j.actaastro.2022.12.035.

[13] T. M. Barrows and J. S. Orr. *Dynamics and Simulation of Flexible Rockets*. Elsevier, 2021. ISBN: 9780128199947. doi: 10.1016/C2019-0-00384-6.

[14] J. A. Macés-Hernández, D. Seelbinder, and S. Theil. Modelling and stability analysis of sloshing on liquid-propelled reusable launch vehicles. 2023. doi: 10.13009/EUCASS2023-549.

[15] F. Capolupo. Equivalent mechanical models for sloshing, 2025. Technical note. doi: 10.48550/ARXIV.2511.10172.

[16] H. W. Bae, K. Geohagan, K. Barber, R. Purandare, and J. Orphee. New perspective on slosh dynamics in high-gravity regimes for lunar missions. In *47th Annual American Astronautical Society (AAS) Guidance, Navigation & Control (GN&C) Conference*, Breckenridge, CO, USA, Feb. 2025.

[17] J. V. Rattayya. Sloshing of liquids in axisymmetric ellipsoidal tanks. In *2nd Aerospace Sciences Meeting*, New York, NY, USA, Jan. 1965. American Institute of Aeronautics and Astronautics. doi: 10.2514/6.1965-114.

[18] D. M. Henderson. Shuttle program. Euler angles, quaternions, and transformation matrices working relationships. NASA Technical Memorandum NASA-TM-74839, NASA, Lyndon B. Johnson Space Center, Houston, TX, USA, July 1977.

[19] N. A. Chaturvedi, A. K. Sanyal, and N. H. McClamroch. Rigid-body attitude control. *IEEE Control Systems Magazine*, 31(3):30–51, 2011. doi: 10.1109/MCS.2011.940459.

[20] J. B. Kuipers. *Quaternions and rotation sequences*. Princeton University Press, Princeton, NJ, 2007. ISBN: 9780691102986.

[21] A. S. Konopliv, R. S. Park, D.-N. Yuan, S. W. Asmar, M. M. Watkins, J. G. Williams, E. Fahnestock, G. Kruizinga, M. Paik, D. Strekalov, N. Harvey, D. E. Smith, and M. T. Zuber. High-resolution lunar gravity fields from the GRAIL primary and extended missions. *Geophysical Research Letters*, 41(5), Mar. 2014. doi: 10.1002/2013gl059066.

[22] T. R. Kane and D. A. Levinson. *Dynamics*. McGraw-Hill, 1985. ISBN: 0070378460.

[23] F. Capolupo and A. Rinalducci. Descent & landing trajectory and guidance algorithms with divert capabilities for moon landing. In *AIAA SCITECH 2024 Forum*. American Institute of Aeronautics and Astronautics, Jan. 2024. doi: 10.2514/6.2024-0086.

[24] T. A. Lance. Analysis of propellant slosh dynamics and generation of an equivalent mechanical model for use in preliminary Voyager autopilot design studies. NASA Contractor Report NASA-CR-95147, Jet Propulsion Laboratory, California Institute of Technology, CA, USA, Dec. 1966.

[25] F. T. Dodge. The new "Dynamic behavior of liquids in moving containers", 2000. Southwest Research Institute, San Antonio, TX, USA.

[26] P. A. C. Mason and S. R. Starin. Propellant slosh analysis for the solar dynamics observatory. NASA Technical Memorandum NASA/TM-2005-213594, Goddard Space Flight Center, Code 595, Greenbelt, MD, USA, July 2005.

[27] E. I. Sumner. Experimentally determined pendulum analogy of liquid sloshing in spherical and oblate-spheroidal tanks. NASA Technical Note NASA-TN-D-2737, NASA Lewis Research Center, Cleveland, OH, USA, April 1965.

[28] A Giordano. Enabling interplanetary exploration for cubesats with a fully chemical propulsion system. *Journal of the British Interplanetary Society*, 76(4), June 2023. doi: 10.59332/jbis-076-04-0134.

[29] G. J. Kim, H. Rhee, W. H. Jeon, J. Jeong, and D.-S. Hwang. Lateral sloshing analysis by CFD and experiment for a spherical tank. *International Journal of Aeronautical and Space Sciences*, 21(3), July 2020. doi: 10.1007/s42405-020-00295-2.